AGU ADVANCING EARTH AND SPACE SCIENCES

Earth and Space Science

RESEARCH ARTICLE
10.1029/2024EA003514

An Evaluation of Low-Cost Terrestrial Lidar Sensors for Assessing Hydrogeomorphic Change

M. T. Perks[1], S. J. Pitman[1], R. Bainbridge[1], A. Díaz-Moreno[1,2], and S. A. Dunning[1]

[1]School of Geography, Politics and Sociology, Newcastle University, Newcastle, UK, [2]JBA Risk Management, Skipton, UK

Key Points:

- Fixed monitoring platforms using small form lidar sensors offer insight into hydrogeomorphic processes at user defined temporal resolution
- Change detection products are within 2–4 cm of those produced using conventional lidar systems at river bank sections
- Application provides quantified insight into bank retreat processes and river water levels at high spatio-temporal resolution

Correspondence to:

M. T. Perks,
matthew.perks@newcastle.ac.uk

Citation:

Perks, M. T., Pitman, S. J., Bainbridge, R., Díaz-Moreno, A., & Dunning, S. A. (2024). An evaluation of low-cost terrestrial lidar sensors for assessing hydrogeomorphic change. *Earth and Space Science*, *11*, e2024EA003514. https://doi.org/10.1029/2024EA003514

Received 10 APR 2024
Accepted 14 JUL 2024

Author Contributions:

Conceptualization: M. T. Perks, S. J. Pitman, R. Bainbridge, A. Díaz-Moreno, S. A. Dunning
Data curation: M. T. Perks
Formal analysis: M. T. Perks, S. J. Pitman, S. A. Dunning
Funding acquisition: M. T. Perks, S. A. Dunning
Investigation: M. T. Perks, S. J. Pitman, S. A. Dunning
Methodology: M. T. Perks, S. J. Pitman, R. Bainbridge, A. Díaz-Moreno, S. A. Dunning
Project administration: M. T. Perks
Resources: M. T. Perks, S. A. Dunning
Software: M. T. Perks, S. J. Pitman
Validation: M. T. Perks, S. J. Pitman
Visualization: M. T. Perks, S. J. Pitman
Writing – original draft: M. T. Perks, S. J. Pitman, R. Bainbridge, A. Díaz-Moreno, S. A. Dunning

Abstract Accurate topographic data acquired at appropriate spatio-temporal resolution is often the cornerstone of geomorphic research. Recent decades have seen advances in our ability to generate highly accurate topographic data, primarily through the application of remote sensing techniques. Structure from Motion-Multi View Stereo (SfM-MVS) and lidar have revolutionised the spatial resolution of surveys across large spatial extents. Technological developments have led to commercialisation of small form factor (SFF) 3D lidar sensors that are suited to deployment on both mobile (e.g., uncrewed aerial systems), and in fixed semi-permanent installations. Whilst the former has been adopted, the potential for the latter to generate data suitable for geomorphic investigations has yet to be assessed. We address this gap here in the context of a 3-month deployment where channel change is assessed in an adjusting fluvial system. We find that SFF 3D lidar sensors generate change detection products comparable to those generated using a conventional lidar system. Areas of no geomorphic change are characterised as such (mean 3D change of 0.014 m compared with 0.0014 m for the Riegl VZ-4000), with differences in median change in eroding sections of between 0.02 and 0.04 m. We illustrate that this data enables: (a) accurate characterisation of river channel adjustments through extraction of bank long-profiles; (b) the assessment of bank retreat patterns which help elucidate failure mechanics; and (c) the extraction of water surface elevations. The deployment of this technology will enable a better understanding of processes across a variety of geomorphic systems, as data can be captured in 4D with near real-time processing.

Plain Language Summary This research demonstrates how instruments that were initially developed for the automotive and robotics industry can be used to provide detailed information about the shape and size of landforms, and how they change over time. The instruments that we use are small, low-cost, lidar sensors (which use laser beams to measure distances). We deployed the sensors over a 3-month period, where they were used to assess how the banks of a river channel changed (eroded and deposited sediment). The river bank of interest was located approximately 30-m away from the lidar sensors and we found them to generate results comparable to those obtained from conventional lidar systems. The small sensors accurately identified areas where no changes occurred, with minor differences in estimates for areas experiencing change. The fixed installation allowed for high-resolution data to be collected every 2-hr. Using this new technology, we were able to accurately study the change of the river channel, measure the patterns of bank retreat, understand the failure mechanisms and extract elevations of the water surface. This new technology has the potential to enhance our understanding of various environments that are undergoing change by capturing detailed data in three-dimensional space over time.

1. Introduction

The development and adoption of remote sensing techniques has undoubtedly been a boon for the geosciences, leading to improvements in our capability to resolve the earth's surface at ever improving spatial and temporal resolutions. Notably, Structure from Motion Multi View Stereo (SfM-MVS), and lidar are widely used to assess fine-scale geomorphic change. These techniques are capable of accurately acquiring thousands of points per minute, covering large spatial extents (often in excess of 1 km^2) and at resolutions generally greater than 10 points per m^2 (Carrivick et al., 2016). However, the frequency with which airborne lidar and SfM-MVS surveys are used at a study location is often limited by resource and time constraints. While ground-based SfM-MVS and lidar have been widely adopted for regular and routine assessments of geomorphic change, the establishment of (semi-) permanent station(s) for data acquisition at high temporal resolution (i.e., sub-daily intervals) over periods of weeks to months is more limited (Figure 1).

Writing – review & editing: M. T. Perks, S. J. Pitman, R. Bainbridge, A. Díaz-Moreno, S. A. Dunning

Up until recently, the acquisition of topographic data at sub-daily intervals using ground-based photogrammetry or lidar has required the installation of costly monitoring infrastructure. Examples of where multiple fixed DSLR time-lapse cameras and SfM-MVS have been used successfully include for the detection of soil erosion (Eltner et al., 2017), and rock slope deformation (Blanch et al., 2021; Kromer et al., 2019). Similarly, semi-permanent 3D lidar systems have been used to elucidate the magnitude-frequency behavior of rockfalls (J. G. Williams et al., 2018), to explore the high-frequency morphodynamics of a sand beach (Anders et al., 2020), and to record surface elevation profiles of debris flows (Aaron et al., 2023). However, perhaps as a consequence of their prohibitive costs, this technology has not been fully exploited to resolve highly transient geomorphic processes or the sequencing of processes across a range of environments.

Recent technological developments are however reducing costs and helping to extend the scope of deployments. For example, very low-cost time-lapse systems have been successfully used to reconstruct glacier calving fronts (Mallalieu et al., 2017; Taylor et al., 2023), and monitor rockfall activity (Blanch et al., 2024), through SfM-MVS reconstructions. Time-of-flight camera systems are an alternative solution for identifying topographic change, however, the spatial resolution and size of the area sensed is typically much smaller compared to time-lapse photogrammetry and lidar (e.g., Grigusova et al., 2022).

Mirroring the recent development of very low cost photogrammetry solutions, advancements in the production of small form factor (SFF) 3D lidar sensors now enable topographic measurements to be acquired at high temporal resolutions (e.g., repeat scans at up to 20 Hz) at relatively low cost. These recently commercialized lidar sensors are designed to be compact (i.e., they have a small form factor) for use in autonomous vehicle navigation (Hecht, 2018; Rapp et al., 2020), mobile robotics (Básaca-Preciado et al., 2014), personal mapping (R. D. Williams et al., 2020), and associated fields. Following the success of integrating these sensors into uncrewed aerial systems (e.g., DJI Zenmuse L1), uncrewed water vehicles (e.g., Sardemann et al., 2018) and into personal mobile devices (e.g., iPhone), these sensors are being deployed in the geosciences to rapidly acquire topographic and vegetation data across large spatial areas (e.g., Gollob et al., 2021; Haddadchi et al., 2023; Luetzenburg et al., 2021; MacDonell et al., 2023). Although Goelles et al. (2022) identified the potential for these small form sensors to be integrated into a fixed system suitable for long-term deployment and capable of acquiring geomorphic data of high spatial and temporal resolution, to date, this has only been explored in the context of snow depth and avalanche monitoring (Kapper et al., 2023; Ruttner-Jansen et al., 2024). Application of these sensors has the potential to improve the quantification of highly transient surface processes (e.g., Aaron et al., 2023), to establish precursors and failure mechanisms of geomorphic events and densify the observational record to facilitate deeper process understanding.

This article therefore seeks to assess the potential for SFF 3D lidar sensors to be installed at a semi-permanent station and to acquire data that is suitable for change detection at the spatial and temporal scales of interest to process geomorphologists. The specific sensor that we use is the Livox Mid-40, which retails for $599 (June 2024 price). This operates at a laser wavelength of 905 nm, with a narrow field of view of 38.4° and a detection range of up to 260 m at 80% reflectivity. The beam divergence is 0.28° (vertical) × 0.03° (horizontal) with a reported angular accuracy of less than 0.1° and a range precision of 0.02 m. Initial evaluations of the Livox Mid-40 sensor indicate range errors below 0.01 m for a range of 37 m and between 0.01 and 0.025 m for a range of 57–130 m (Ortiz Arteaga et al., 2019). Whilst these specifications are not comparable to conventional lidar systems, they are likely acceptable to most process geomorphologists and potentially an upgrade on current surveying capabilities where high-frequency data capture is of paramount importance. To establish the utility of these sensors for assessing geomorphic change we:

1. Produce and test a workflow for automated alignment of data acquired from two Livox Mid-40 sensors operating simultaneously.
2. Assess the consistency between geomorphic change detection products derived using the Livox Mid-40 sensor and a conventional lidar system (Riegl VZ-4000).
3. Use these data to gain insight into the hydrogeomorphic processes occurring in an actively adjusting river system during a 3-month monitoring period.

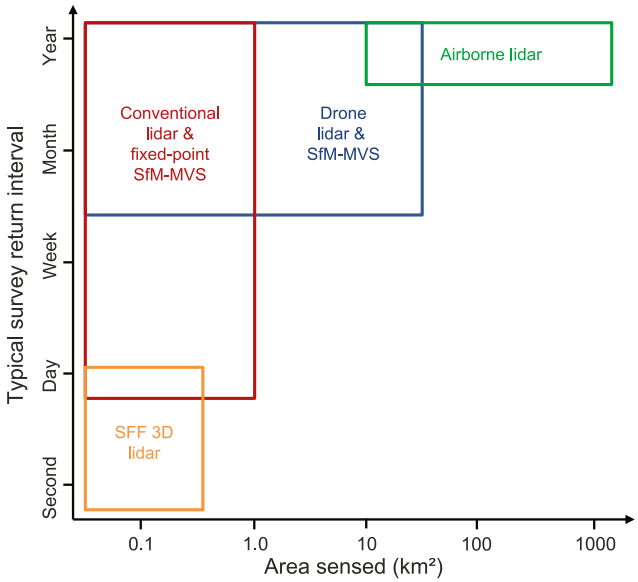

Figure 1. Available surface elevation data sources acquired at high spatial resolution (sub-meter or better) in context of the area typically sensed and typical return intervals between surveys.

2. Methods

2.1. Study Site

This research is focused on Goldrill Beck, a 38 km^2 predominantly upland catchment in Cumbria (UK). In 2021, the river was the subject of a flagship restoration project commissioned by the National Trust, Europe's biggest conservation charity. The in-stream works were designed to transform the embanked, straightened single-thread channel into a more complex form well connected with its floodplain. Given the recent completion of the restoration works, dynamic equilibrium between channel form and in-stream process has yet to be established. As such, the upper sections of the restored reach have undergone significant adjustment, particularly during periods of elevated flows. There has been a reorganization of the channel and the development of a steep-faced point bar which has created a more dynamic flow field, and initiated erosion of the outer bank (Figure 2). This area is the focus of monitoring with a SFF 3D lidar sensing system, detailed in the subsequent section.

2.2. Instrumentation

The monitoring platform adopted for this case study consists of two main components, namely: (a) power supply infrastructure and; (b) SFF 3D lidar system. The power supply consists of 4 × 120 Ah 12v batteries wired in parallel maintained by a 100°W solar panel. The 12v supply is fed to the lidar sensing system through an electronic timing unit to control the power supply. The sensing system consists of a controller unit (Fitlet 2 equipped with an Atom x7-E3950 processor and 16 GB RAM), and two Livox Mid-40 lidar sensors synchronized by a Livox Hub (Livox, 2019). The total cost of the system was $5,300, with the power supply infrastructure accounting for $1,500 of this.

The two Livox Mid-40 lidar sensors were installed to provide a 60° horizontal field of view across the area of interest with a 17° overlap between the two individual scanners for data alignment purposes. Each lidar sensor is capable of emitting 100,000 laser pulses per second and they were programmed to collect data simultaneously for 60-s. Field tests carried out in the present study show that scanning of a river bank face oriented orthogonal to the sensor at a distance of 30 m for 60-s results in the acquisition of a point cloud with a surface density in excess of 6,000 points per m^2. The Livox Mid-40 scanner publishes its data at 20 Hz with the "rosette" non-repetitive scan pattern ensuring that the point cloud densifies with time. Scans were scheduled to occur at 2-hr intervals throughout the day, and the data were stored locally. This survey schedule was selected following an evaluation of the anticipated rate of change at this particular location balanced with the power demands of the system. These raw data are stored in a proprietary (.lvx) data format with a size of ≈170 Mb per scan interval. This is subsequently converted to a single .pcd file using the Robot Operating System (ROS) prior to splitting, alignment, and analysis (Figure 3).

A 3-axis accelerometer is installed within the sensing system enclosure to determine its relative movement during lidar acquisition periods. The sensor is based on the ADXL345 IC and is capable of providing high resolution (13-bit) measurement at up to ±16 g (Analog Devices, 2022). Data are acquired at a rate of 200 Hz concurrently alongside the Livox Mid-40 data. Using these data, the magnitude of acceleration [m s^{-2}] was calculated from each three-axial acceleration sample. Subsequently, the vector magnitude is fed a Bandpass-filter with a passband frequency range of 30–80 Hz to remove the gravitational component and low frequency noise. Cutoff frequencies were selected after the analysis of the power spectrum of the FFT series. From this filtered series, we calculate the root mean square and use this as the metric for describing sensor movement.

2.3. Alignment and Adjustment Procedures

The approach adopted for alignment and adjustment of scan data into a consistent coordinate system relies on two assumptions: (a) data acquired from scanner01 and scanner02 contain sufficient tie-points in the overlapping regions to enable internal adjustment, and (b) that stable reference features across the domain are present to enable

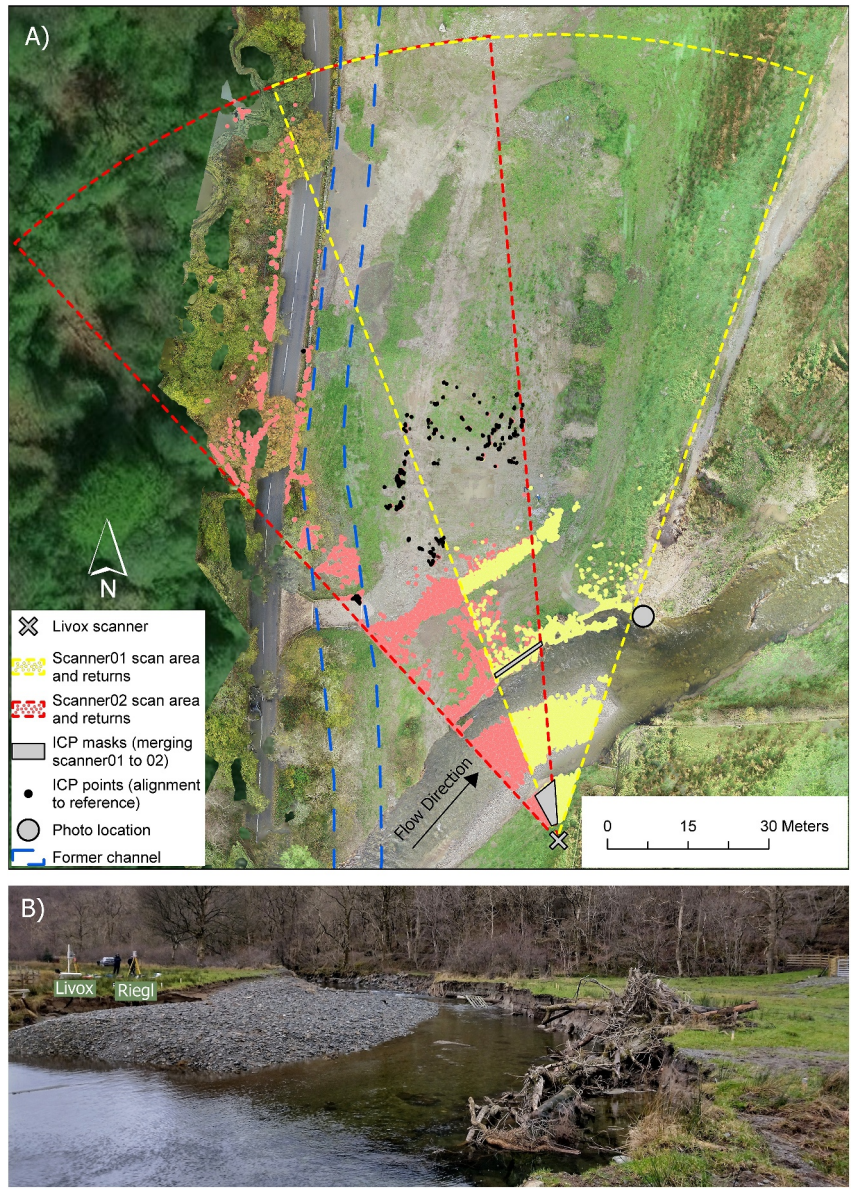

Figure 2. (a) Upper reach of the modified Goldrill Beck showing imagery acquired by UAS on 10th November 2021 (4-months after realignment completion). The photo displayed in Figure 1b is taken looking upstream from the gray circle in Figure 1a. In this image the locations of Livox Mid-40 and Riegl VZ-4000 scanning systems are on the true right bank.

the merged scans for each epoch to be referenced to the initial pose of the system. The workflow for implementing these approaches is outlined below, and illustrated in Figure 3.

The first phase of alignment requires the projection of data acquired from scanner01 into the same physical space as scanner02 for each epoch, as both are collected in an instrument-centric system. The adjustment for each epoch is determined on an individual basis, that is, the adjustment is not assumed to be constant through time. This was achieved first through an automated coarse alignment, which broadly registered the two scans. Subsequently, two patches in the near field of the overlapping scan regions were selected and fine-registered using an iterative closest point (ICP) algorithm in the command line interface of CloudCompare v2.12.1 (Figure 3). The two sections chosen for this alignment were exposed vegetation and gravel proximal to the scanner, and exposed bank on the far side of the river channel (Figure 2). These patches have multiple orientations (horizontal and vertical surfaces, respectively) that aid in the point matching procedure and improve geometric stability (Gelfand et al., 2003). Following calculation of the 3D transformation matrix for projecting scanner01 into scanner02 space, this was

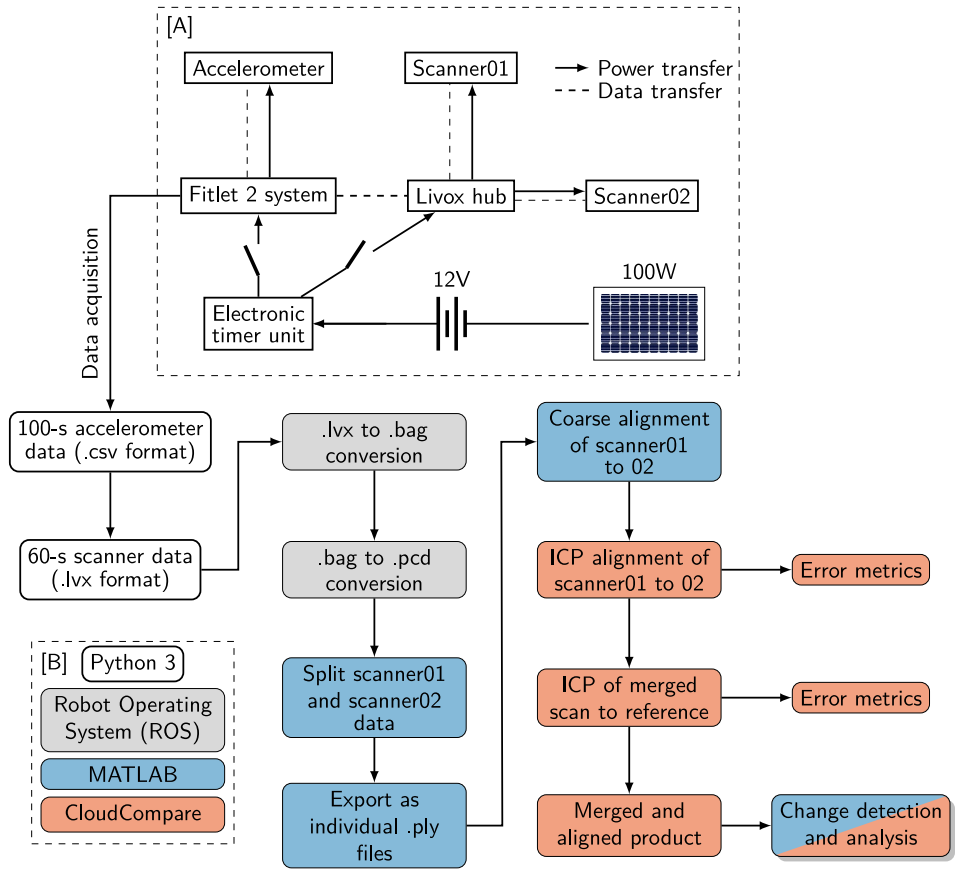

Figure 3. Schematic diagram illustrating the workflow for data acquisition, alignment and adjustment. Items in (a) represent the sensor and data acquisition setup, with the subsequent processing workflow presented below. The processing software used for each stage is color-coded based on the legend presented in (b).

applied, resulting in the generation of the newly aligned scanner01, and an internally consistent merged product (scanner01 and scanner02).

Following the initial alignment, alignment of the merged scans for each epoch with the initial pose of the system (determined on 29th January 2022) was achieved by selecting features from three patches distributed throughout the domain (Figure 2). As we align each epoch with a reference scan obtained at the start of the sampling period, the selected features should be stable. Therefore, permanent structures and natural features that are not exposed to fluvial activity are selected. These features are a fence (located to the left extreme of the scanned region at a distance of 50 m from the scanner), a telegraph pole located 100 m away from the scanner, and finally exposed gravel and boulders in the central portion of the domain in the mid-distance (50 m from the scanner).

2.4. Validation Data Acquisition

Given the novel adoption of the Livox Mid-40 lidar sensor to assess geomorphic change, we present data acquired using a Riegl VZ-4000 (Riegl LMS GmbH, 2020), during the active monitoring period for comparison purposes. The Riegl VZ-4000 is a conventional terrestrial laser scanner with a precision and accuracy of 10 and 15 mm, respectively, at a distance of 150 m (Riegl LMS GmbH, 2020). The scans were acquired on 28th January 2022 and on 24th March 2022. These surveys took place on the day before data acquisition with the Livox Mid-40 system began and coincided with the final day of data acquisition with the Livox Mid-40 system. The reference Riegl VZ-4000 scans are acquired in close proximity to the Livox Mid-40 system. The first scan was acquired at a horizontal and vertical distance of 4.7 and +0.28 m relative to the Livox Mid-40 system and the later scan was acquired at a horizontal and vertical distance of 6.0 and +0.36 m relative to the Livox Mid-40 system. The later scan was aligned to the first scan through ICP within RiScan Pro v2.8 (alignment error <0.01 m) before being clipped to the

Table 1
Point Cloud Characteristics and Parameters Used in M3C2 Data Processing

Measurement					
System	Date	Mean point density [pts m^{-2}]	D [m]	d [m]	Search length [m]
Riegl VZ-4000	28 January 2022	10,000[a]	0.325	0.20	3.86
Riegl VZ-4000	24 March 2022	11,800[a]	0.325	0.20	3.86
Livox Mid-40	29 January 2022	4,300	0.325	0.20	3.86
Livox Mid-40	24 March 2022	4,200	0.325	0.20	3.86

Note. Point density is averaged from across the entire region of interest (including water surface). This value therefore underestimates the point density in the areas where change is being assessed. [a]Riegl VZ-4000 data has been sub-sampled from the original resolution to a maximum point density of 20,000 pts. m^{-2}.

region of interest and sub-sampled to a maximum point density of 20,000 pts m^{-2} in order to reduce the very high density of the point cloud, particularly in the near field.

2.5. Comparison With Validation Data

Detection of geomorphic change for the period 28th January–24th March 2022 using data acquired by the Riegl VZ-4000 TLS was determined using the M3C2 plugin within CloudCompare (Lague et al., 2013). M3C2 leverages the benefits of fully 3D point clouds rather than simplification to surfaced 2.5D models. The patterns and magnitude of the detected change are then compared with the change detected using the Livox Mid-40 system between 29th January 2022 and 24th March 2022. The application of the M3C2 algorithm (Lague et al., 2013) for change detection involves first the calculation of the local normal vector of the (earliest) point cloud by fitting a plane to the points within a radius of D/2, where D is greater than the local roughness elements. This parameter should be sufficiently large to guarantee that the distance measurement is independent of the surface roughness, but large enough to capture the surface geometry, for example, transitions from floodplain to bank-face (Zahs et al., 2022). Values for D have ranged from ≈0.1 to ≫2 m in previous studies (Barnhart & Crosby, 2013; DiFrancesco et al., 2020; Haddadchi et al., 2023; Lague et al., 2013; Stumpf et al., 2015). In this study, D was defined as the mean of point cloud roughness multiplied by 25 as recommended by Lague et al. (2013). The projection scale d over which each cloud is averaged is calculated by assessing point cloud density with d being defined to include a minimum of 20 points with $d < D$ (Lague et al., 2013). The maximum search length was defined to ensure that all change within the region of interest could be detected. A summary of the parameters used in these calculations can be found in Table 1.

2.6. Change Detection

2.6.1. Water Level Extraction

Sensing water surface elevations, while acquiring topographic information on the spatial scale of interest for this study, poses a significant challenge. Although lidar sensors have been used successfully to acquire accurate water surface elevation data in field studies, their deployment is limited to a narrow range of operating conditions. This is primarily due to water strongly attenuating the signal at the wavelengths that lidar sensors typically operate (e.g., 905 nm) (Wojtanowski et al., 2014), which is compounded by the phenomenon that calm water may behave as a specular surface, which produces reflections instead of dispersing incipient energy back to the sensor (Paul et al., 2020). Therefore, one of the primary considerations is that the strength of the return signal is strongest when the sensor is located close to the water surface, oriented at nadir, and sensing turbulent flows. Such a sensor configuration would limit the spatial extent of the sensed area and significantly reduce the ability to detect bank-normal geomorphic change. Therefore, in order to estimate water levels across flow magnitudes, whilst sensing the wider topography, in an unsupervised workflow, an alternative approach is adopted. The fundamental assumption of this approach is that the near-field point density will be greatest in the terrestrial environment and that this will reduce markedly when it transitions into the occupied river channel (Figure 4a). This is clearly demonstrated in Figure 4b where we observe few returns in the river channel and many on the bank that defines the channel edge. By determining the position and elevation of this point density threshold change we are able to estimate water surface elevations without relying on returns from the water surface itself—in effect we identify

10.1029/2024EA003514

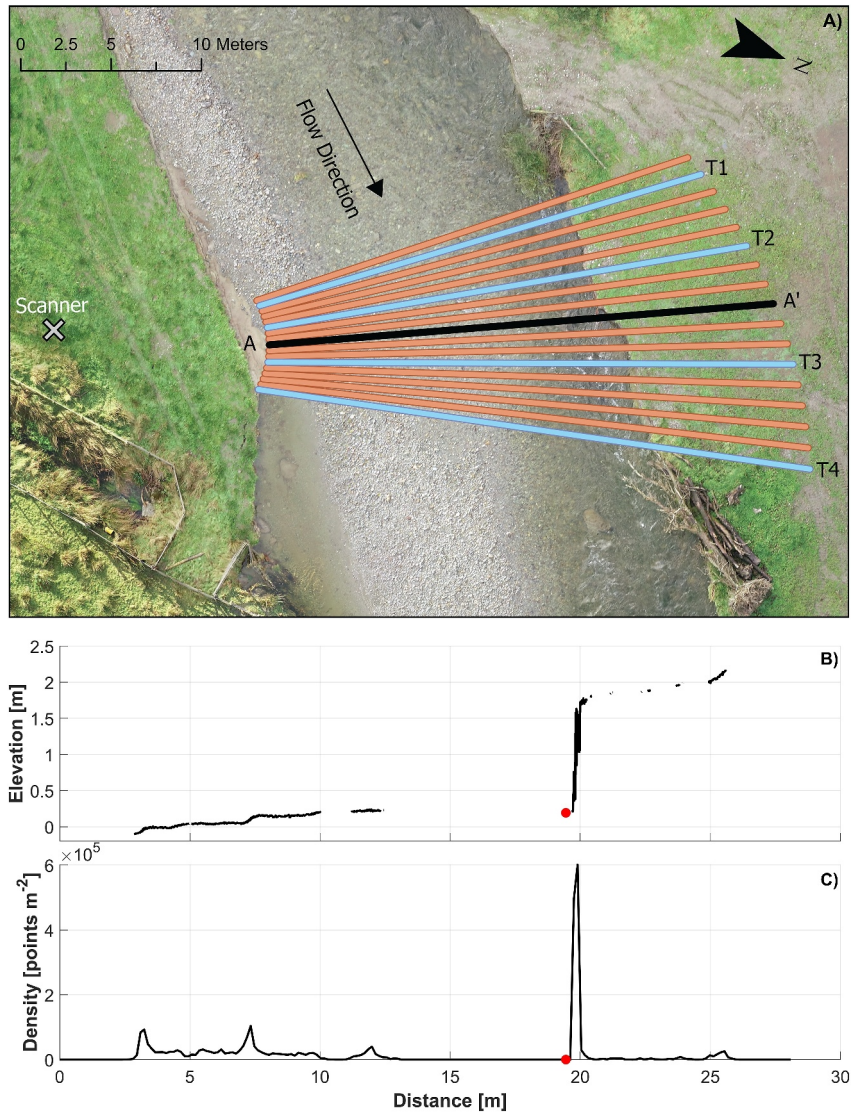

Figure 4. (a) Orthophoto generated from a UAS SfM-MVS survey on 10th November 2021 showing the region of interest. Search lines used for determining water extent and river level are colored red (see Section 3.3.1). The blue lines (labeled T1–T4) represent locations used for the extraction of the water level and are also used to examine the style and rates of geomorphic change during a period of high flow (see Section 3.3). Point-cloud data are extracted along the black A–A′ line and are displayed in (b) and (c). These illustrate how the elevation of the point returns vary (panel b) and how the density along the transect is influenced by the material being detected (panel c). The red dots in (b) and (c) represent the local minima of impulse returns, which are used to delineate the elevation of the water surface.

the boundary between the densely captured sub-vertical bank and the sparse/zero return water surface (Figure 4c). The high density point cloud enables us to extract an average of more than 6,000 points from each cross-sectional slice to determine the transition from terrestrial to inundated areas. This local minima search procedure is implemented at 15 cross sections through the bank and channel, with data within 0.05 m of these lines being used in this analysis. We initially seed the algorithm with an estimated location of the deepest part of the channel, where we are confident there will always be water present, and from there search away from the lidar toward the bank. Working with these data, we identify the location along the transect where returns increase above zero and extract points along the transect within 0.5 m of this location. We finally calculate the 5th percentile of the extracted heights, which is used for the water level observations for each individual scan epoch. This approach has the benefits of enabling topographic change to be determined across a large region of interest, whilst extracting supplementary information about water surface elevations. Comparisons are made between the Livox Mid-40-

extracted water levels with those made by an In Situ Aqua TROLL 200 Data Logger housed within a stilling well 225 m upstream of the area sensed by the Livox Mid-40 system. To allow comparison between reported water heights, upstream water levels are found for each corresponding Livox Mid-40 measurement, and a constant offset of +0.13 m is applied to the pressure transducer water heights to bring them in line with the Livox Mid-40 coordinate system.

2.6.2. Geomorphic Change Detection

Geomorphic change detection was undertaken on the merged and adjusted point clouds between 29th January 2022 and 23rd March 2022 with the analysis focusing on assessing the change on the sub-vertical true left river bank. Firstly, long profiles of the bank position at an elevation of between 1.2 and 1.3 m (approximately mid bank height) are extracted. Each 19 m long profile consists of over 100,000 data points, and these are extracted every 7-days. Variance with a moving window of five samples is calculated, with data being removed when the local variance exceeds 0.1 m. Subsequently, the data was smoothed using a Gaussian-weighted moving average filter with window size of five. Following the initial weekly evaluation we undertook more detailed analysis on a time period where we identified significant change to have occurred. Specifically, we analyse each scan acquired between 18th–22nd February 2022, which is a period characterised by elevated river flow conditions. We examine change at four sections that intersect the bank (labeled T1–T4 in Figure 4a). Using a swath width of 0.1 m we extract point positions in bins of 0.1 m increments at heights spanning 0.8–2.00 m with the central position (X and Y coordinates) of each bin being determined following k-means cluster analysis.

3. Results

3.1. Alignment and Adjustments

ICP alignment between scanner01 and scanner02 was generally successful with a mean RMSE of 0.016 m and a standard deviation of 0.001 m (Figure 5a). Deviations in the RMSE are asynchronous with periods of increased sensor movement indicating that the alignment process is robust to small changes in pose during acquisition (e.g., those associated with wind effects). Despite this apparent consistency, the lidar system's pose does change during the sampling period. Between 29th January 2022 and 23rd March 2022 the mean translation components are 0.01, 0.025, and 0.01 m for X, Y, and Z respectively, whereas for the subsequent period up to 30th April 2022 the corresponding values are −0.001, 0.075, and 0.03 m for X, Y, and Z components respectively (Figure 5b). A similar step-change can be observed in the rotation angle on 23rd March 2022 (Figure 5c). This shift corresponds with a period of site maintenance and although the position and orientation of the sensors were not knowingly adjusted, the change in transformation parameters indicates otherwise. Importantly, the workflow adopted is able to cope with these abrupt changes and compensate appropriately. When the data are considered as two separate periods the consistency of the necessary adjustments is evident, with standard deviations in the translation components of 0.003, 0.0047, 0.0055 m for X, Y, and Z, respectively, in the first period (up to 23rd March 2022) and of 0.006, 0.0086, 0.01 m, respectively, for the period spanning 23rd March 2022–30th April 2022.

ICP alignment between the merged scan for each epoch and the original reference scan was broadly successful with a mean RMSE of 0.026 m and a standard deviation of 0.046 m (Figure 5d). However, it should be noted that this RMSE is nearly double that of the initial ICP alignment, with a four-fold increase in the standard deviation. This is perhaps unsurprising given that this phase of the registration process seeks to align scans acquired several weeks and months apart using only natural features within the scanners field-of-view. In fact, previous work has illustrated that ICP registration will not produce high-precision registration (i.e., <1 cm) in a natural environment (Lague et al., 2013). The increase in RMSE over time indicates that the feature matching process becomes less robust over time, with a maximum RMSE of 0.0475 m on 22nd March 2022, and a trend of generally increasing RMSE values after 16th April 2022. Similarly to internal alignment (scanner01 to scanner02), deviations in the RMSE are asynchronous with periods of increased sensor movement, as revealed by the accelerometer data (Figure 5d). Apparent changes in the lidar system's pose are less obvious in this instance, because of the increased noise in the translation parameters. This is exemplified in the standard deviations of the translation components of 0.02, 0.013, 0.041 m for X, Y, and Z, which are an order of magnitude greater than for the internal alignment procedure (Figure 5e). Although there is also increased noise in the rotational components, these data are more consistent with standard deviations in X, Y, and Z of 0.066°, 0.041°, and 0.038° respectively. It should also be noted that after the maintenance visit of 23rd March 2022, a shift in angular rotations can be detected (Figure 5f).

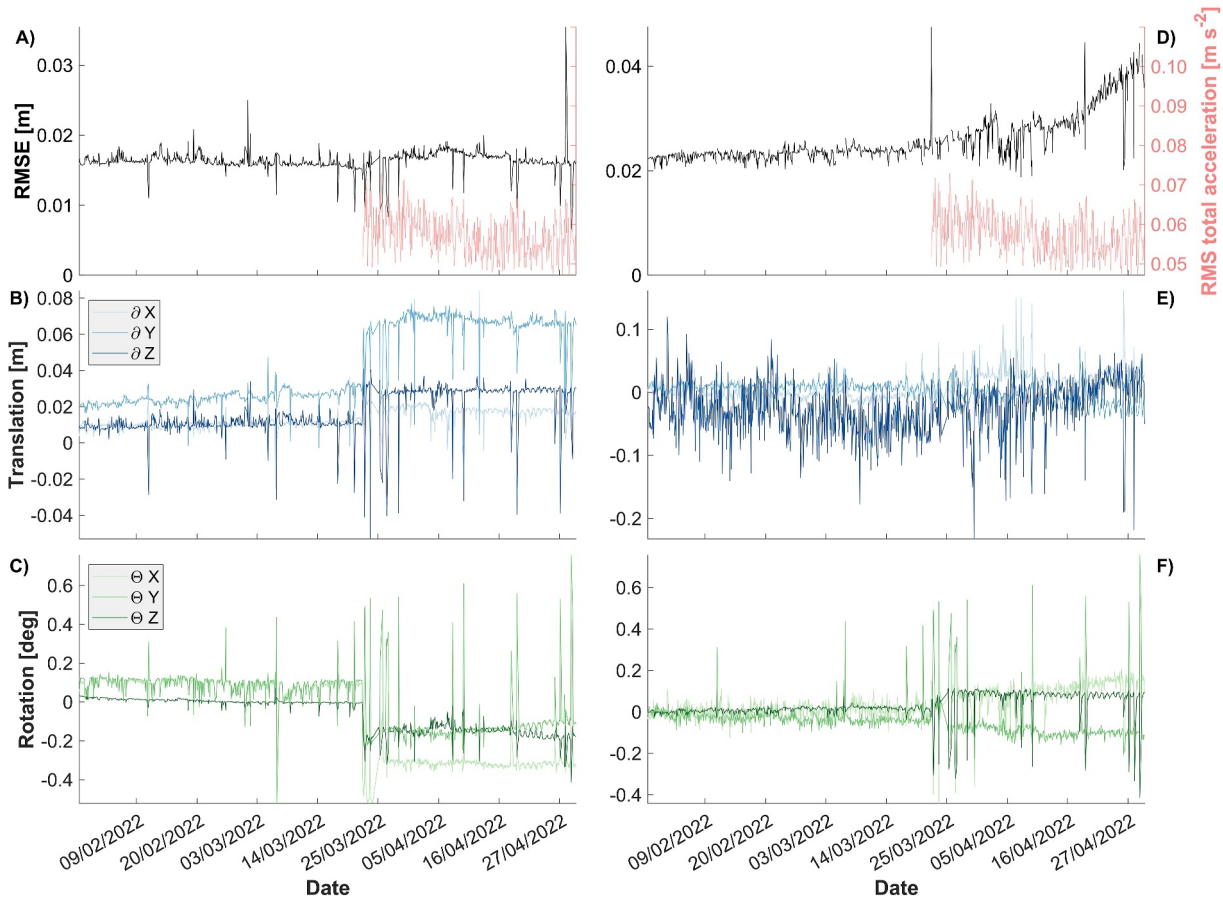

Figure 5. Data describing the outputs from ICP alignment of scanner01 to scanner02 for each epoch (a–c) and the outputs from ICP alignment of each merged scan to the reference scan obtained on 29th January 2022 (d–f). The RMSE following alignment is shown (black) alongside the RMS of the total acceleration monitored using an tri-axial accelerometer (red) (a and d). Individual axis translation (b and e) and rotation (c and f) components obtained from the 3D matrix transformation following ICP.

3.2. Validation

Areas within the field of view where we expect no topographic change to have occurred (e.g., the floodplain beyond the far bank of the river) exhibit mean elevation change of 0.014 m for the Livox Mid-40 and 0.0014 m for the Riegl VZ-4000. There is also consistency in the documented patterns of channel bank activity with significant erosion to the left of the region of interest (Zone 1 in Figure 6), and a mixture of no change and variable erosion rates in the center (Zones 2 and 3 in Figure 6). The area to the right of Zone 3 is particularly complex, as documented erosion is largely the result of large woody debris entering the channel from the bank side immediately upstream (visible in Figures 2b and 4a), which is subsequently transported downstream during the monitoring period. As such there are areas of significant erosion (woody debris removal) but also some areas of no change (parts of the channel bank). Therefore, our focus is on the analysis of change within Zones 1–3 (Figures 6 and 7). Qualitatively, we can observe that the change detection products produced using the Livox Mid-40 and Riegl VZ-4000 point clouds appear to be broadly consistent with corresponding areas of erosion and deposition (Figure 6). However, there is greater variability in the Riegl VZ-4000 change detection products compared with those generated using the Livox Mid-40 point cloud, with the latter being more gradual across each zone. We can also observe that Livox Mid-40 M3C2 change detection is not identified in the lower extent of Zone 1 and 2 and in the center of Zone 3, whereas the change detection data are more complete for the Riegl VZ-4000 data.

Upon closer analysis of the change detected by the Livox Mid-40 and Riegl VZ-4000 sensors, we can see that the median M3C2 change values for Zones 1–3 are −0.98, −0.02, and −0.41 m for the Livox Mid-40, and −0.96, 0.00, −0.45 m for the Riegl VZ-4000 that is, differences in median change estimates range from 0.02 to 0.04 m in the three zones (Figure 7). The interquartile range values for Zones 1–3 are 0.45, 0.03, and 0.46 m for the Livox

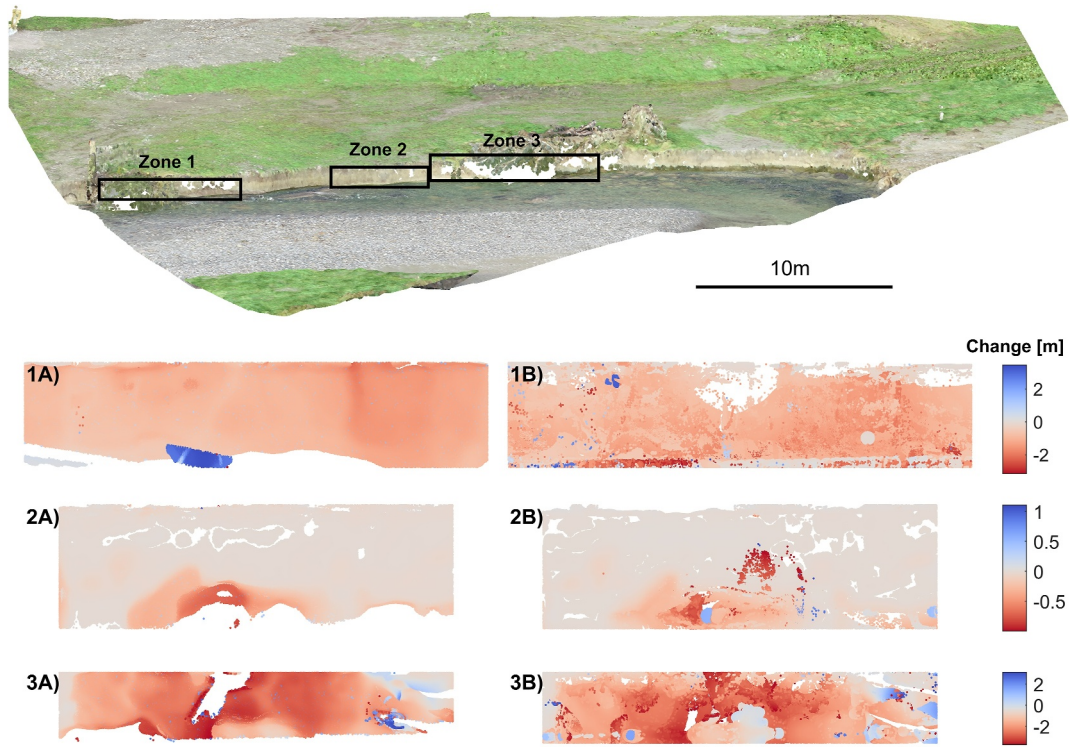

Figure 6. Colored point cloud point generated from a UAS SfM-MVS survey on 10th November 2021 showing the region of interest. View is from the true right bank across to the true left (i.e., the scanner view). Rectangles labeled Zone 1–3 indicate the approximate locations where the Livox Mid-40 and Riegl VZ-4000 M3C2 change detection products are extracted. Change in Zone 1–3 are shown for the Livox Mid-40 in subplots labeled (1a–3a), and (1b–3b) for the Riegl VZ-4000. Change is presented for the period spanning 29th January 2022 to 24th March 2022 for the Livox Mid-40, and the period spanning 28th January 2022 to 24th March 2022 for the Riegl VZ-4000.

Mid-40, and 0.50, 0.06, 0.49 m for the Riegl VZ-4000; the difference in IQRs between the two systems range from 0.03 to 0.05 m illustrating that the spread of central portion of the data are reasonably consistent between the two systems. However, deviations can be seen at the lower and upper extremes of the cumulative distribution plots (Figure 7), with the Riegl VZ-4000 having a tendency to detect higher magnitudes of erosion in all three zones. This analysis illustrates that data acquired from the Livox Mid-40 and Riegl VZ-4000 lidar systems are capable of producing broadly consistent change detection products.

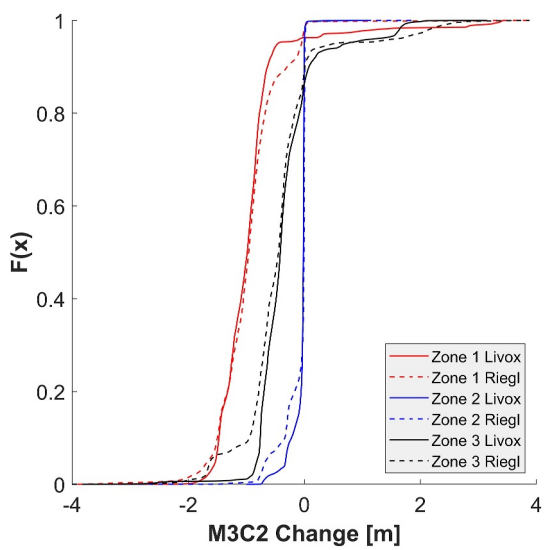

Figure 7. Empirical cumulative distribution plots of the M3C2 change detected between 28th January 2022 and 24th March 2022 within zones 1–3 as shown in Figure 6.

3.3. Change Detection

Here, we illustrate the utility of the Livox Mid-40 sensors for detecting geomorphic change. We begin by showing how river level can be indirectly estimated from lidar returns (Section 3.3.1), followed by an assessment of the style and magnitude of bank retreat throughout the monitoring period and a closer look at erosion dynamics during a high flow event (Section 3.3.2).

3.3.1. Water Level Extraction

The Livox Mid-40 method accurately estimates low and normal flow conditions with the 5th and 50th percentiles of the Livox Mid-40 and gauging station measurements being 0.177 and 0.314 m versus 0.195 and 0.326 m. The root mean square error of the Livox Mid-40 measurements at water levels up to the 50th and 90th percentiles is 0.028 and 0.033 m, respectively. Under these conditions, the flow stage estimates from the Livox Mid-40 compare

10.1029/2024EA003514

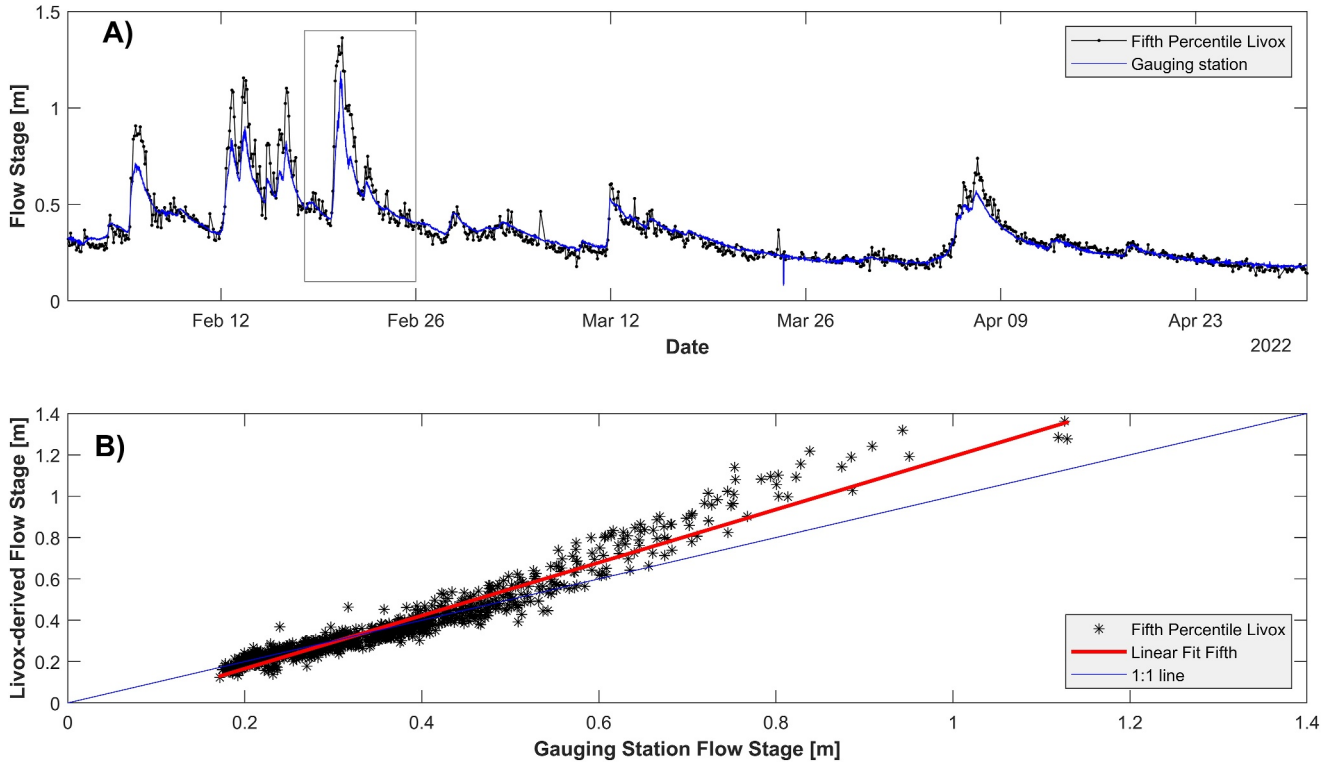

Figure 8. (a) Time series of flow data between 29th January 2022 and 30th April 2022, derived from the Livox Mid-40 scans (black line) and compared against a gauging station located 225 m upstream (blue line). The gray box identifies the time period of detailed analysis undertaken in Section 3.3.2 and presented in Figure 9. (b) A direct scatter comparison of the Livox Mid-40 and gauging station values.

reasonably favorably with the measurements from the gauging station (Figure 8a). Under elevated flow conditions (>90th percentile), flow estimates are over-predicted by the Livox Mid-40 as shown by a 95th percentile value of 0.801 m compared to 0.65 m for the gauged station. Furthermore, the absolute peak of high-flow events typically returns values around 0.2–0.3 m higher than at the gauging station. This is evident in the scatter of Livox Mid-40 versus gauging station flow data (Figure 8b), where the linear fit ($R^2 = 0.97$) diverges from the 1:1 line. However, this is not necessarily the result of erroneous measurements by the Livox Mid-40 system. This overestimation relative to the upstream gauge may be due to the presence of high flow velocities on the approach to a 50° right bend immediately upstream of the sensed area (Figure 2). Under these conditions, the surface of the river water has a transverse slope, resulting in variable elevations of the water for a given cross section (Chow, 1986). To illustrate this, we use the approach presented in Graf and Altinakar (1998, p. 104) to estimate the maximum superelevation with an approach velocity of 1.33 m s^{-1} (which is the highest depth-averaged velocity recorded by ADCP at the site). It is estimated that these conditions would lead to a maximum superelevation of 0.29 m. Therefore, this indicates that the velocity head $\left(\frac{V^2}{2g}\right)$ and the channel geometry at the sensed location may be a major factor in determining the discrepancy between the Livox Mid-40 stage measurements and the upstream gauged data under high flow conditions.

3.3.2. Bank Retreat

Extraction of the bank long-profile at 7-day intervals shows the spatially non-uniform and time-dependent nature of the channel change across the area (Figure 9). At the start of the monitored period the bank position is stable, however, we begin to detect the first signs of retreat on 12th February. Initially this is highly localized, for example, we can detect small-scale erosion of the order of 0.3 m occurring between 15 and 16 m (X-axis position; Figure 9a). We are also able to identify how initial erosion can have subsequent impacts on adjacent patches. Immediately downstream of 15–16 m (X position) we begin to observe progressive erosion totaling ≈0.6 m by 19th February. By 26th February there has been widespread change. For example, between 5.5 and 12.5 m (X

10.1029/2024EA003514

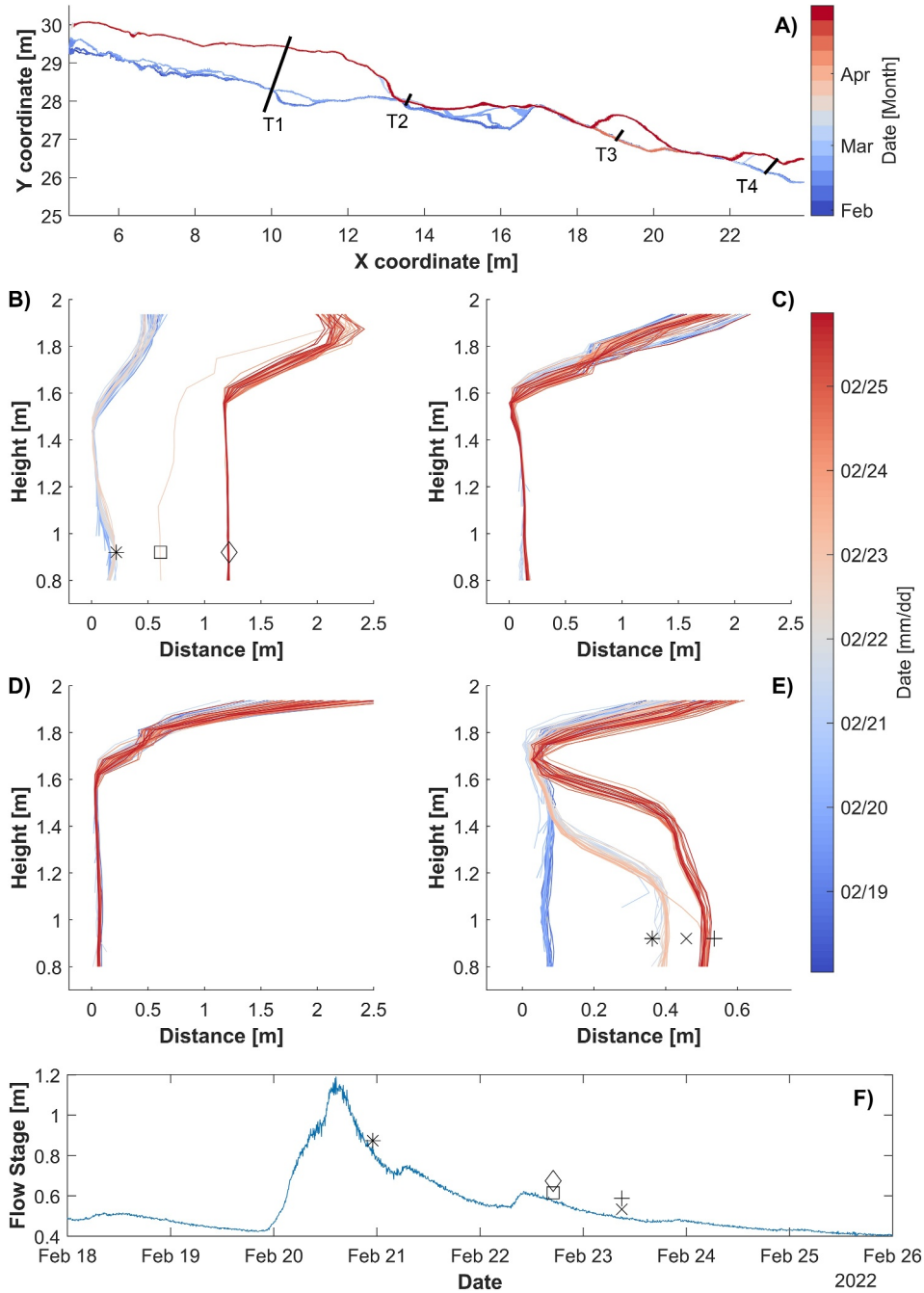

Figure 9. (a) Nadiral view showing river bank position along a 19m long profile as detected by the Livox Mid-40 sensors between 29th January 2022 and 30th April 2022. Bank positions are presented at bank heights of 1.2–1.3 m (approximately mid-bank) at 7-day intervals. Transects labeled T1–T4 correspond to the same transect names shown in Figure 4. Data for T1–T4 are extracted at 2-hr intervals between 18 and 26th February and presented in (b–e). The black symbols in (b–e) correspond to the timing and flow stage of the symbols in (f). These symbols are referred to in Section 3.3.2. Flow stage measurements are derived from the pressure transducer (see Section 2.6.1) and correspond to approximate heights present across the sensed area.

position) there is further erosion of ≈1 m, bringing the total retreat to ≈1.4 m in places. However, we can also identify that specific locations along the transect are resistant to erosion despite adjustments occurring upstream and downstream. This can be observed at 13 m (*X* position), where there is very little retreat throughout the monitoring period, despite total retreat immediately downstream being of the order of 0.5 m. Analysis of the point

cloud at this stable location shows the presence of a large boulder (with dimensions of at least $1.3 \times 0.8 \times 0.25$ m) embedded in the toe of the bank, which appears to prevent erosion from occurring. The data presented also illustrate that periods of limited activity are adequately characterized as such. For example, there is little erosion along the transect throughout most of March with the bank face seemingly stabilizing. Indeed, rates of erosion decline throughout this period and into April with the exception of retreat between 18 and 20 m (X position) of the order of 0.6 m.

As described above, the 19th–26th February represents a period of major adjustment along considerable portions of the long profile. Next we will explore the style of this change using the full resolution data series available (acquired at 2-hr intervals). Transects T1 and T4 experience change most acutely (Figure 9). In the case of T1 (Figure 9b), we can identify that between 18th and 20th February there is negligible change despite the peak river flows occurring during this time period. Indeed, erosion does not begin to occur until river flows begin to subside. Between 21st and 22nd February the toe of the bank undergoes small-scale erosion, that is, < 0.1 m erosion at a height of 0.8–1.2 m (black star in Figure 9b). At 5 p.m. on 22nd February, there is the first of two dramatic retreats. The first is of the order of 0.4 m on the bank toe, 0.7 m on the middle bank, and 1.5 m on the top of the bank (black square in Figure 9b). By 7 p.m. the toe of the bank has retreated an additional 0.6 m, the mid-bank a further 0.5 m and the position of the bank-top has begun to stabilize (black diamond in Figure 9b). These two failures occur within a 4-hr period at a relatively moderate flow stage of $\approx$0.6 m, considering that the peak flow stage 2-days earlier reached 1.19 m (Figure 9f).

In the case of T4 (Figure 9e), we can identify that, similar to T1, there is negligible change until 20th February at 23:00 when the lower and mid-bank (0.8–1.3 m height) retreat by 0.3 m (black star in Figure 9e). The location of the upper bank (1.3–2m) is stable despite the presence of a significant cut at the bank toe. This leads to a period of stability until the erosion of the toe begins on 23rd February at 9 a.m., with a further 0.1 m of retreat occurring at heights of 0.8–1.00 m (black cross in Figure 9e). By 11 a.m. this has extended upward, leading to retreat occurring up to a bank height of 1.6 m (black plus sign in Figure 9e). This period of instability again occurs during low magnitude and falling flow conditions following peak flows on 20th February (Figure 9f).

In contrast to transects T1 and T4 which experience significant adjustments, T2 and T3 are stable during this period of elevated flow conditions (Figures 9c and 9d). The position of the vertical bank face is precisely resolved with a position range of 1–2 cm. However, beyond the vertical face, there appear to be higher levels of noise in the data. At these positions, the surface is $<10°$ from horizontal, resulting in a greater incidence angle between the sensor and the surface. Given this scanning geometry, we expect the relative signal level of the measurements to be reduced and the beam footprint to become elongated, which may lead to increases in the standard error (Soudarissanane et al., 2011).

4. Discussion

4.1. Enhanced Process Understanding

Our analysis of time periods that undergo significant retreat finds evidence of shear-type bank collapse (Figure 9b), undercutting, and tensile failures (Figure 9e). These are observed to occur during falling river levels, or once the levels have receded to baseflow. During these times the river level is below the point of failure. These dynamics are indicative of bank collapse processes dominating as a consequence of fluctuations in soil pore water pressure and seepage flow, as opposed to near-bank hydrodynamics leading to fluvial entrainment.

In the case where we observe undercutting and tensile failures (Figure 9e), the height of the bank that undergoes initial failure is likely to have been submerged under maximum water level conditions. In such cases, the switch from submerged to saturated conditions can result in a doubling of the bulk unit weight of the soil, and the unloading of the lateral support provided by elevated water levels can lead to block instability (Lawler, Thorne, & Hooke, 1997; Pinyol et al., 2008). Furthermore, as the cohesive soils transition from saturated conditions to unsaturated conditions there will be decreasing hydrostatic pressure head but excess pore-water pressure which potentially contributes to failure (Francalanci et al., 2013; Zhao et al., 2022). In the case where we observe shear-type bank collapse (Figure 9b), we observe very minor undercutting initially followed by rapid retreat and vertical collapse of the bank face during the receding limb of the hydrograph. In contrast to undercutting and tensile failures, these shear-type bank collapses have been shown to be a result of delays in the development of high pore water pressures in the soil which reduce friction and cohesion of the block (Deng et al., 2018; Lawler, Thorne, &

Hooke, 1997). However, we also observe a significant retreat in the cohesive upper part of the riverbank (Figure 9b). This was not submerged during peak flows and may indicate the importance of erosion by seepage flow (e.g., Fox & Wilson, 2010). Even during a single high-flow event, we observe differing styles of retreat across the area being sensed. Given the heterogeneous nature of the bank material (incorporating both gravel and cohesive sediments), further research will utilise the high resolution data to elucidate drivers such as the timing and sequencing of flow events (e.g., cycles of wetting and drying), and whether bank properties (e.g., geometry and structure of the bank, and saturation levels inferred from point intensity data), can provide additional insight into the failure mechanics observed.

4.2. Gaps in High-Frequency Sensing Capabilities for Geomorphic Research

Although traditional surveying approaches (Global navigation satellite system (GNSS), total stations) can provide highly accurate topographic measurements, there are limits to the spatio-temporal information that can be acquired with these systems, for example, they are often periodic or point based (Montillet et al., 2024). Existing remote sensing methods also have limitations. For example, although SfM-MVS has been successfully adopted to constrain erosion rates using UASs, the need for an operator to be present provides a limit to the potential re-visit frequency. Similarly, whilst automated SfM-MVS systems can be deployed from pillar and pole mounts at distances of beyond 250 m (e.g., Blanch et al., 2023), the resolution of their products in the far-field diminishes and there are considerations related to automated camera alignment and georeferencing that need to be overcome in a continuous deployment (e.g., Blanch et al., 2021). Where near-real-time data are desired, the computational demands of SfM-MVS must also be considered. Such deployments require significant processing power locally or sufficient bandwidth to allow high resolution imagery to be processed in the cloud, or servers remote from the field site as outlined in Blanch et al. (2021, 2023). Alternatively, the costs associated with survey-grade 3D lidar sensors are often prohibitive to their long-term deployment unless sites justify the expenditure based on, for example, direct risks posed. SFF 3D lidar sensors, such as the Livox Mid-40 sensors, presented in this article will help to fill the gap in our ability to generate topographic products at high spatial resolution for the detection of centimeter-scale changes at a range of several tens of meters. They also enable frequent surveys (hourly intervals or better), that can be achieved rapidly, in an automated workflow at low-cost. Across sub-disciplines of the geosciences this is a limiting factor to generating new process understanding, which we will explore in the following section.

4.3. Wider Implications for Geomorphic Research

In fluvial systems, bank erosion is recognized as a key contributor to fine sediment fluxes (Walling, 2005; Walling et al., 2003). Through dedicated efforts and the deployment of erosion pins, the assessment of bank erosion rates at the catchment level has been possible (e.g., Kronvang et al., 2013). Although this provides spatial patterns and valuable sediment flux information, information related to the failure mechanisms can be missed using these approaches. Alternative efforts, using bank-side sensors such as Photo-electronic erosion pin (PEEP) systems (Lawler, Couperthwaite, et al., 1997) offer high temporal resolution descriptors of bank retreat, however, these point measurements limit the density of bank-side observations. Detailed understanding of the precursors, and failure mechanisms may be poorly understood due to the spatio-temporal sampling frequencies of current approaches particularly in rapidly changing environments for example, in ice-affected rivers within and outside periglacial landscapes (Chassiot et al., 2020).

Similarly, landslide strain patterns and precursors to failure are often investigated using point measurements, such as extensometers, inclinometers, or GNSS. In some cases high-cost conventional lidar units have been deployed to allow better spatio-temporal patterns of change (J. G. Williams et al., 2018) or strain (Kromer et al., 2017) to be quantified, but this is not the norm. This limits our understanding of the drivers and responses of hillslopes to forcing (rainfall, for example) and often impacts our ability to determine sequences of events and magnitude-frequencies of change, as both are linked to survey frequencies as change detection is time-integrated between survey epochs (J. G. Williams et al., 2018). Such gaps could be addressed through deployment of SFF 3D lidar sensors at fixed locations.

In soil erosion assessments very few studies measure the water erosion response at the scales 0.01–100 ha. Research on sheet and rill erosion rates and controls is usually obtained from small runoff plots with most slope lengths shorter than 50 m (Maetens, Poesen, & Vanmaercke, 2012; Maetens, Vanmaercke, et al., 2012). There is a

gap in our understanding at these scales, where erosion mechanisms may transition from being dominated by interrill and rill processes to the potential formation of gullies (Poesen, 2018). Hillslopes of these dimensions would be within the range of 1–2 pole-mounted scanning systems that could offer frequent (i.e., subhourly), high-resolution (subdecimeter) data sets. Of consideration here however is the importance of scanning geometry which is critical during deployment of these sensors (as shown in Section 3.3.2). The angle of incidence between the sensor and the surface should be minimized, which may pose a technical challenge on gently sloping hillsides, which may be characteristic of many agricultural environments.

In coastal process research, 2D lidar (e.g., SICK LMS511) is being used to analyse geomorphic change at a temporal resolution not typically accessible hitherto. In practice, this means that wave-by-wave sediment fluxes and transport can be quantified on beach foreshores (Almeida et al., 2020), the time-varying free water surface in the swash zone can be measured and used to quantify swash-front gradients and the presence of bores (Blenkinsopp et al., 2010), and measurement of the transformation of breaking waves in the surfzone has also been possible when the instrumentation is mounted on piers and jetties (Martins et al., 2017). However, the limited spatial footprint of 2D lidar systems has resulted in multiple units being deployed side by side to resolve morphological change that varies in 3D (i.e., has alongshore variability in addition to cross-shore change). Such an approach was adopted by Pitman et al. (2024) where two SICK LMS511 units were situated 10 m apart to track changes in beach cusps. The 3D nature of the Livox Mid-40 units negate this need for multiple proximal units whilst operating at a temporal resolution that still enables wave-by-wave processes to be quantified (a cost saving in excess of $15,000). Newer versions of the Livox such as the AVIA model also allow the user to select non-repetitive (area) or repetitive (profile line/quasi-2D) scanning, rivaling the ability of the SICK systems. Furthermore, the Livox Mid-40 offers a much improved range (90 m at 10% reflectivity) compared to the SICK (40 m at 10% reflectivity), which proves critical on low reflectivity surfaces such as gravels.

4.4. Technology Adoption Pathways

The key challenges to adopting autonomous remote sensing tools for geomorphic research include innovation in platform development and processing workflows (Tomsett & Leyland, 2019). The platform we describe is designed to be deployed in semi-permanent installations where an advantageous configuration would yield high-resolution data for a specific area undergoing adjustment. The system is designed to be deployed off-grid and can be powered by 12v batteries and maintained by small-scale renewables. In instances where power supply is a severely limiting factor, data may be stored locally for download and processing at a later date, or alternatively transmitted to remote servers for processing using the workflow described. The system is entirely modular enabling components to be switched depending on the requirements of the survey. For example, the Livox Mid-40 may be switched with a sensor with a larger field of view (e.g., Livox AVIA @ 70°), or for one with a longer range (e.g., Livox Tele-15 @ 500 m). The current draw during scan acquisition is estimated to be 200W (180W Livox Hub, 10W Livox Mid-40, 10W Fitlet2), which is significant. However, given that Livox Mid-40 sensors can acquire 12 million data points during a 1-min scan, acquisition times and power draw per day can be limited. Data processing (including conversion, splitting, alignment, and merging, as illustrated in Figure 3) can typically be completed in seconds to a few minutes. The time taken scales with the size and complexity of the area being sensed, as well as the adjustments required. The time required to perform these tasks can be further reduced through workflow optimization. For example, rather than use of natural features to align the scan positions, the deployment of retro-reflective or high reflective Lambertian targets at fixed positions would speed up the alignment and remove the need for ICP adjustment (e.g., Goelles et al., 2022). Efficiency gains may also be made by using alternative pose estimation methods such as those using point-to-edge and point-to-plane scan-matching algorithms (e.g., Shan & Englot, 2018), and deep learning architecture (e.g., Gojcic et al., 2019). There are also opportunities for harmonization with existing software packages (e.g., Goelles et al., 2021), and the optimization of processing workflows for deployment across a range of geomorphic environments should be the focus of future research.

5. Conclusions

In this study, we investigate the potential for small form factor lidar sensors to be installed at a semi-permanent station to acquire data that is suitable for change detection at the spatial and temporal scales of interest to process geomorphologists. To achieve this, we establish a monitoring platform equipped with Livox Mid-40 lidar sensors and monitor an actively adjusting reach of Goldrill Beck (UK) for a period of 3-months. Following analysis of

data generated across this monitoring period and following comparison with data sets generated using conventional lidar systems and an upstream flow gauging station, we can draw the following conclusions:

1. Small form lidar sensors such as the Livox Mid-40 can be embedded within a fixed, semi-permanent monitoring platform to acquire 3D topographic data autonomously.
2. Multiple sensors can be integrated into a single platform and be adequately aligned resulting in RMSE values of <0.02 m. The success of alignment back to a reference scan using natural features is achievable but with RMSE values of up to 0.04 m over a 3-month period. Adoption of a network of retro reflective or high reflective Lambertian targets will improve alignment procedures in future applications.
3. Across a 3 month period, areas of no geomorphic change are adequately characterized as such (mean change of 0.014 m compared with 0.0014 m for the Riegl VZ-4000). Assessment of geomorphic change at three zones in the actively eroding bank face show differences in median change estimates of 0.02–0.04 m between survey platforms.
4. River water levels can be indirectly estimated across the field-of-view with an RMSE of 0.04 m (up to the 90th percentile) when compared with measurements made at an upstream gauging station. Deviations between the lidar derived water surface elevations and gauged data occur under high flow conditions. Our analysis indicates this is likely a result of superelevation of the water profile which opens the potential for the sensors to be used to resolve non-uniform flow dynamics in river channels and open-water.
5. Over a 3-month period we observe bank erosion in excess of 1 m across large swathes of the sensed area. However, across the 19 m transect, change is spatially non-uniform with some areas experiencing no detectable change. The timing of erosion is also highly variable. Whilst the largest erosion events occur during the same time period (i.e., during flow recession following a period of high flow), some areas are resistant to change during this time period only to fail at a later date. Across the sensed area, the primary erosion mechanisms were mass failure of the block following a period of high flow.
6. Wider deployment and application of this emerging, new technology will enable better process understanding across a variety of geomorphic systems.

Data Availability Statement

Software used for the acquisition and processing of lidar data from the Livox Mid-40 sensing system, and code for the generation of Figures can be found in Perks (2024). Data used in the production of Figures can be found in Perks et al. (2023). Links to the raw Livox Mid-40 data can be found in Perks (2024).

Acknowledgments
This research was supported by the National Trust through the "Monitoring the hydro-geomorphic response of the Goldrill Beck realignment" project. We thank the National Trust and Howe Green Farm for arranging access and granting permissions to undertake this work. SD, and AM recognize funding from "Pitch-In," part of Research England's Connecting Capability Fund (CCF). This research article was greatly improved following feedback from several anonymous reviewers, Dr Thomas Gölles, and Prof. Mikaël Attal.

References

Aaron, J., Spielmann, R., McArdell, B. W., & Graf, C. (2023). High-frequency 3D lidar measurements of a debris flow: A novel method to investigate the dynamics of full-scale events in the field. *Geophysical Research Letters*, *50*(5), e2022GL102373. https://doi.org/10.1029/2022GL102373

Almeida, L. P., Almar, R., Blenkinsopp, C., Senechal, N., Bergsma, E., Floc'h, F., et al. (2020). Lidar observations of the swash zone of a low-tide terraced tropical beach under variable wave conditions: The Nha Trang (Vietnam) COASTVAR experiment. *Journal of Marine Science and Engineering*, *8*(5), 302. https://doi.org/10.3390/jmse8050302

Analog Devices. (2022). *adxl345*. Analog Devices. (Revision G). Retrieved from https://www.analog.com/media/en/technical-documentation/data-sheets/adxl345.pdf

Anders, K., Winiwarter, L., Lindenbergh, R., Williams, J. G., Vos, S. E., & Höfle, B. (2020). 4d objects-by-change: Spatiotemporal segmentation of geomorphic surface change from lidar time series. *ISPRS Journal of Photogrammetry and Remote Sensing*, *159*, 352–363. https://doi.org/10.1016/j.isprsjprs.2019.11.025

Barnhart, T. B., & Crosby, B. T. (2013). Comparing two methods of surface change detection on an evolving thermokarst using high-temporal-frequency terrestrial laser scanning, Selawik River, Alaska. *Remote Sensing*, *5*(6), 2813–2837. https://doi.org/10.3390/rs5062813

Básaca-Preciado, L. C., Sergiyenko, O. Y., Rodríguez-Quinonez, J. C., García, X., Tyrsa, V. V., Rivas-Lopez, M., et al. (2014). Optical 3D laser measurement system for navigation of autonomous mobile robot. *Optics and Lasers in Engineering*, *54*, 159–169. https://doi.org/10.1016/j.optlaseng.2013.08.005

Blanch, X., Eltner, A., Guinau, M., & Abellan, A. (2021). Multi-epoch and multi-imagery (MEMI) photogrammetric workflow for enhanced change detection using time-lapse cameras. *Remote Sensing*, *13*(8), 1460. https://doi.org/10.3390/rs13081460

Blanch, X., Guinau, M., Eltner, A., & Abellan, A. (2023). Fixed photogrammetric systems for natural hazard monitoring with high spatio-temporal resolution. *Natural Hazards and Earth System Sciences*, *23*(10), 3285–3303. https://doi.org/10.5194/nhess-23-3285-2023

Blanch, X., Guinau, M., Eltner, A., & Abellan, A. (2024). A cost-effective image-based system for 3D geomorphic monitoring: An application to rockfalls. *Geomorphology*, *449*, 109065. https://doi.org/10.1016/j.geomorph.2024.109065

Blenkinsopp, C., Mole, M., Turner, I., & Peirson, W. (2010). Measurements of the time-varying free-surface profile across the swash zone obtained using an industrial lidar. *Coastal Engineering*, *57*(11), 1059–1065. https://doi.org/10.1016/j.coastaleng.2010.07.001

Carrivick, J. L., Smith, M. W., & Quincey, D. J. (2016). *Structure from motion in the geosciences*. John Wiley & Sons.

Chassiot, L., Lajeunesse, P., & Bernier, J.-F. (2020). Riverbank erosion in cold environments: Review and outlook. *Earth-Science Reviews*, *207*, 103231. https://doi.org/10.1016/j.earscirev.2020.103231

Chow, V. (1986). *Open-channel hydraulics*. McGraw-Hill.
Deng, S., Xia, J., Zhou, M., Li, J., & Zhu, Y. (2018). Coupled modeling of bank retreat processes in the upper Jingjiang Reach, China. *Earth Surface Processes and Landforms*, *43*(14), 2863–2875. https://doi.org/10.1002/esp.4439
DiFrancesco, P.-M., Bonneau, D., & Hutchinson, D. J. (2020). The implications of M3C2 projection diameter on 3D semi-automated rockfall extraction from sequential terrestrial laser scanning point clouds. *Remote Sensing*, *12*(11), 1885. https://doi.org/10.3390/rs12111885
Eltner, A., Kaiser, A., Abellan, A., & Schindewolf, M. (2017). Time lapse structure-from-motion photogrammetry for continuous geomorphic monitoring. *Earth Surface Processes and Landforms*, *42*(14), 2240–2253. https://doi.org/10.1002/esp.4178
Fox, G. A., & Wilson, G. V. (2010). The role of subsurface flow in hillslope and stream bank erosion: A review. *Soil Science Society of America Journal*, *74*(3), 717–733. https://doi.org/10.2136/sssaj2009.0319
Francalanci, S., Bendoni, M., Rinaldi, M., & Solari, L. (2013). Ecomorphodynamic evolution of salt marshes: Experimental observations of bank retreat processes. *Geomorphology*, *195*, 53–65. https://doi.org/10.1016/j.geomorph.2013.04.026
Gelfand, N., Ikemoto, L., Rusinkiewicz, S., & Levoy, M. (2003). Geometrically stable sampling for the icp algorithm. In *Fourth International Conference on 3-D Digital Imaging and Modeling, 2003. 3DIM 2003. Proceedings* (pp. 260–267).
Goelles, T., Hammer, T., Muckenhuber, S., Schlager, B., Abermann, J., Bauer, C., et al. (2022). Molisens: Mobile lidar sensor system to exploit the potential of small industrial lidar devices for geoscientific applications. *Geoscientific Instrumentation, Methods and Data Systems*, *11*(2), 247–261. https://doi.org/10.5194/gi-11-247-2022
Goelles, T., Schlager, B., Muckenhuber, S., Haas, S., & Hammer, T. (2021). pointcloudset: Efficient analysis of large datasets of point clouds recorded over time. *Journal of Open Source Software*, *6*(65), 3471. https://doi.org/10.21105/joss.03471
Gojcic, Z., Zhou, C., Wegner, J. D., & Wieser, A. (2019). The perfect match: 3D point cloud matching with smoothed densities. In *Proceedings of the IEEE/CVF Conference on Computer Vision and Pattern Recognition* (pp. 5545–5554).
Gollob, C., Ritter, T., Kraßnitzer, R., Tockner, A., & Nothdurft, A. (2021). Measurement of forest inventory parameters with apple iPAD pro and integrated lidar technology. *Remote Sensing*, *13*(16), 3129. https://doi.org/10.3390/rs13163129
Graf, W. H., & Altinakar, M. S. (1998). *Fluvial hydraulics: Flow and transport processes in channels of simple geometry*. Wiley.
Grigusova, P., Larsen, A., Achilles, S., Brandl, R., del Río, C., Farwig, N., et al. (2022). Higher sediment redistribution rates related to burrowing animals than previously assumed as revealed by time-of-flight-based monitoring. *Earth Surface Dynamics*, *10*(6), 1273–1301. https://doi.org/10.5194/esurf-10-1273-2022
Haddadchi, A., Bind, J., Hoyle, J., & Hicks, M. (2023). Quantifying the contribution of bank erosion to a suspended sediment budget using boat-mounted lidar and high-frequency suspended sediment monitoring. *Earth Surface Processes and Landforms*, *48*(14), 2920–2938. https://doi.org/10.1002/esp.5667
Hecht, J. (2018). Lidar for self-driving cars. *Optics & Photonics News*, *29*(1), 26–33. https://doi.org/10.1364/OPN.29.1.000026
Kapper, K. L., Goelles, T., Muckenhuber, S., Trügler, A., Abermann, J., Schlager, B., et al. (2023). Automated snow avalanche monitoring for Austria: State of the art and roadmap for future work. *Frontiers in Remote Sensing*, *4*, 1156519. https://doi.org/10.3389/frsen.2023.1156519
Kromer, R. A., Abellán, A., Hutchinson, D. J., Lato, M., Chanut, M.-A., Dubois, L., & Jaboyedoff, M. (2017). Automated terrestrial laser scanning with near-real-time change detection—Monitoring of the séchilienne landslide. *Earth Surface Dynamics*, *5*(2), 293–310. https://doi.org/10.5194/esurf-5-293-2017
Kromer, R. A., Walton, G., Gray, B., Lato, M., & Group, R. (2019). Development and optimization of an automated fixed-location time lapse photogrammetric rock slope monitoring system. *Remote Sensing*, *11*(16), 1890. https://doi.org/10.3390/rs11161890
Kronvang, B., Andersen, H. E., Larsen, S. E., & Audet, J. (2013). Importance of bank erosion for sediment input, storage and export at the catchment scale. *Journal of Soils and Sediments*, *13*(1), 230–241. https://doi.org/10.1007/s11368-012-0597-7
Lague, D., Brodu, N., & Leroux, J. (2013). Accurate 3D comparison of complex topography with terrestrial laser scanner: Application to the Rangitikei canyon (N-Z). *ISPRS Journal of Photogrammetry and Remote Sensing*, *82*, 10–26. https://doi.org/10.1016/j.isprsjprs.2013.04.009
Lawler, D. M., Couperthwaite, J., Bull, L. J., & Harris, N. M. (1997). Bank erosion events and processes in the upper Severn basin. *Hydrology and Earth System Sciences*, *1*(3), 523–534. https://doi.org/10.5194/hess-1-523-1997
Lawler, D. M., Thorne, C. R., & Hooke, J. M. (1997). Bank erosion and instability. In *Applied fluvial geomorphology for river engineering and management* (pp. 137–172).
Livox. (2019). Livox mid series: User manual. Retrieved from https://www.livoxtech.com/3296f540ecf5458a8829e01cf429798e/downloads/Livox%20Mid%20Series%20User%20Manual%20EN%2020190118.pdf.Livox
Luetzenburg, G., Kroon, A., & Bjørk, A. A. (2021). Evaluation of the apple iPhone 12 Pro lidar for an application in geosciences. *Scientific Reports*, *11*(1), 22221. https://doi.org/10.1038/s41598-021-01763-9
MacDonell, C. J., Williams, R. D., Maniatis, G., Roberts, K., & Naylor, M. (2023). Consumer-grade UAV solid-state lidar accurately quantifies topography in a vegetated fluvial environment. *Earth Surface Processes and Landforms*, *48*(11), 2211–2229. https://doi.org/10.1002/esp.5608
Maetens, W., Poesen, J., & Vanmaercke, M. (2012). How effective are soil conservation techniques in reducing plot runoff and soil loss in Europe and the Mediterranean? *Earth-Science Reviews*, *115*(1), 21–36. https://doi.org/10.1016/j.earscirev.2012.08.003
Maetens, W., Vanmaercke, M., Poesen, J., Jankauskas, B., Jankauskiene, G., & Ionita, I. (2012). Effects of land use on annual runoff and soil loss in Europe and the Mediterranean: A meta-analysis of plot data. *Progress in Physical Geography: Earth and Environment*, *36*(5), 599–653. https://doi.org/10.1177/0309133312451303
Mallalieu, J., Carrivick, J. L., Quincey, D. J., Smith, M. W., & James, W. H. (2017). An integrated structure-from-motion and time-lapse technique for quantifying ice-margin dynamics. *Journal of Glaciology*, *63*(242), 937–949. https://doi.org/10.1017/jog.2017.48
Martins, K., Blenkinsopp, C. E., Power, H. E., Bruder, B., Puleo, J. A., & Bergsma, E. W. (2017). High-resolution monitoring of wave transformation in the surf zone using a lidar scanner array. *Coastal Engineering*, *128*, 37–43. https://doi.org/10.1016/j.coastaleng.2017.07.007
Montillet, J.-P., Kermarrec, G., Forootan, E., Haberreiter, M., He, X., Finsterle, W., et al. (2024). How big data can help to monitor the environment and to mitigate risks due to climate change: A review. *IEEE Geoscience and Remote Sensing Magazine*, *12*, 2–24. https://doi.org/10.1109/MGRS.2024.3379108
Ortiz Arteaga, A., Scott, D., & Boehm, J. (2019). Initial investigation of a low-cost automotive lidar system. *The International Archives of the Photogrammetry, Remote Sensing and Spatial Information Sciences*, *XLII-2/W17*, 233–240. https://doi.org/10.5194/isprs-archives-XLII-2-W17-233-2019
Paul, J. D., Buytaert, W., & Sah, N. (2020). A technical evaluation of lidar-based measurement of river water levels. *Water Resources Research*, *56*(4), e2019WR026810. https://doi.org/10.1029/2019WR026810
Perks, M. (2024). Catchmentsci/livox-poc-article: Release v1.0. *Zenodo*. https://doi.org/10.5281/zenodo.12095181
Perks, M., Dunning, S., Bainbridge, R., Pitman, S., & Díaz-Moreno, A. (2023). Data for output replication. https://doi.org/10.25405/data.ncl.23501091.v2

Pinyol, N. M., Alonso, E. E., & Olivella, S. (2008). Rapid drawdown in slopes and embankments. *Water Resources Research*, *44*(5). https://doi.org/10.1029/2007WR006525

Pitman, S. J., Coco, G., Hart, D. E., & Shulmeister, J. (2024). Observations of beach cusp morphodynamics on a composite beach. *Geomorphology*, *447*, 109026. https://doi.org/10.1016/j.geomorph.2023.109026

Poesen, J. (2018). Soil erosion in the anthropocene: Research needs. *Earth Surface Processes and Landforms*, *43*(1), 64–84. https://doi.org/10.1002/esp.4250

Rapp, J., Tachella, J., Altmann, Y., McLaughlin, S., & Goyal, V. K. (2020). Advances in single-photon lidar for autonomous vehicles: Working principles, challenges, and recent advances. *IEEE Signal Processing Magazine*, *37*(4), 62–71. https://doi.org/10.1109/MSP.2020.2983772

Riegl LMS GmbH. (2020). Riegl vz-4000 data sheet. Retrieved from http://www.riegl.com/uploads/tx_pxpriegldownloads/RIEGL_VZ-4000_Datasheet_2020-09-14.pdf

Ruttner-Jansen, P., Voordendag, A., Hartmann, T., Glaus, J., Wieser, A., & Bühler, Y. (2024). Monitoring snow depth variations in an avalanche release area using low cost lidar and optical sensors. *EGUsphere*, *2024*, 1–20. https://doi.org/10.5194/egusphere-2024-744

Sardemann, H., Eltner, A., & Maas, H.-G. (2018). Acquisition of geometrical data of small rivers with an unmanned water vehicle. *The International Archives of the Photogrammetry, Remote Sensing and Spatial Information Sciences*, *XLII-2*, 1023–1027. https://doi.org/10.5194/isprs-archives-XLII-2-1023-2018

Shan, T., & Englot, B. (2018). Lego-loam: Lightweight and ground-optimized lidar odometry and mapping on variable terrain. In *IEEE/RSJ International Conference on Intelligent Robots and Systems (IROS)* (pp. 4758–4765).

Soudarissanane, S., Lindenbergh, R., Menenti, M., & Teunissen, P. (2011). Scanning geometry: Influencing factor on the quality of terrestrial laser scanning points. *ISPRS Journal of Photogrammetry and Remote Sensing*, *66*(4), 389–399. https://doi.org/10.1016/j.isprsjprs.2011.01.005

Stumpf, A., Malet, J.-P., Allemand, P., Pierrot-Deseilligny, M., & Skupinski, G. (2015). Ground-based multi-view photogrammetry for the monitoring of landslide deformation and erosion. *Geomorphology*, *231*, 130–145. https://doi.org/10.1016/j.geomorph.2014.10.039

Taylor, L. S., Quincey, D. J., & Smith, M. W. (2023). Evaluation of low-cost raspberry pi sensors for structure-from-motion reconstructions of glacier calving fronts. *Natural Hazards and Earth System Sciences*, *23*(1), 329–341. https://doi.org/10.5194/nhess-23-329-2023

Tomsett, C., & Leyland, J. (2019). Remote sensing of river corridors: A review of current trends and future directions. *River Research and Applications*, *35*(7), 779–803. https://doi.org/10.1002/rra.3479

Walling, D. (2005). Tracing suspended sediment sources in catchments and river systems. *The Science of the Total Environment*, *344*(1), 159–184. https://doi.org/10.1016/j.scitotenv.2005.02.011

Walling, D., Collins, A., & McMellin, G. (2003). A reconnaissance survey of the source of interstitial fine sediment recovered from salmonid spawning gravels in England and wales. *Hydrobiologia*, *497*(1/3), 91–108. https://doi.org/10.1023/a:1025413721647

Williams, J. G., Rosser, N. J., Hardy, R. J., Brain, M. J., & Afana, A. A. (2018). Optimising 4-D surface change detection: An approach for capturing rockfall magnitude–frequency. *Earth Surface Dynamics*, *6*(1), 101–119. https://doi.org/10.5194/esurf-6-101-2018

Williams, R. D., Lamy, M.-L., Maniatis, G., & Stott, E. (2020). Three-dimensional reconstruction of fluvial surface sedimentology and topography using personal mobile laser scanning. *Earth Surface Processes and Landforms*, *45*(1), 251–261. https://doi.org/10.1002/esp.4747

Wojtanowski, J., Zygmunt, M., Kaszczuk, M., Mierczyk, Z., & Muzal, M. (2014). Comparison of 905 nm and 1550 nm semiconductor laser rangefinder's performance deterioration due to adverse environmental conditions. *Opto-Electronics Review*, *22*(3), 183–190. https://doi.org/10.2478/s11772-014-0190-2

Zahs, V., Winiwarter, L., Anders, K., Williams, J. G., Rutzinger, M., & Höfle, B. (2022). Correspondence-driven plane-based M3C2 for lower uncertainty in 3D topographic change quantification. *ISPRS Journal of Photogrammetry and Remote Sensing*, *183*, 541–559. https://doi.org/10.1016/j.isprsjprs.2021.11.018

Zhao, K., Coco, G., Gong, Z., Darby, S. E., Lanzoni, S., Xu, F., et al. (2022). A review on bank retreat: Mechanisms, observations, and modeling. *Reviews of Geophysics*, *60*(2), e2021RG000761. https://doi.org/10.1029/2021RG000761